

# Highly Active and Stable Single-Atom Cu Catalysts Supported by a Metal–Organic Framework

Ali M. Abdel-Mageed,<sup>†,‡,§</sup> Bunyarat Rungtaweeworant,<sup>‡,§,#</sup> Magdalena Parlinska-Wojtan,<sup>||</sup> Xiaokun Pei,<sup>‡,§</sup> Omar M. Yaghi,<sup>\*,‡,§,¶</sup> and R. Jürgen Behm<sup>\*,†,¶</sup>

<sup>†</sup>Institute of Surface Chemistry and Catalysis, Ulm University, D-89069 Ulm, Germany

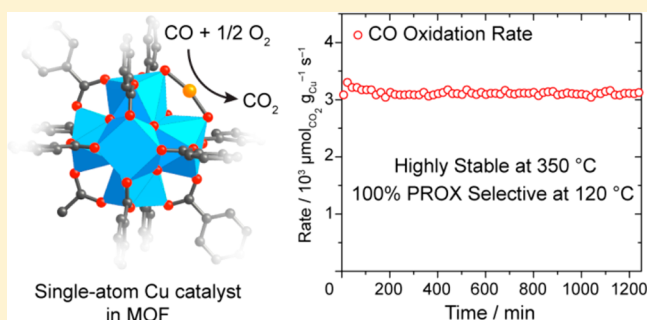
<sup>‡</sup>Department of Chemistry and Kavli Energy NanoSciences Institute, University of California—Berkeley, Berkeley, California 94720, United States

<sup>§</sup>Materials Sciences Division, Lawrence Berkeley National Laboratory, Berkeley, California 94720, United States

<sup>||</sup>Institute of Nuclear Physics, Polish Academy of Sciences, Krakow 31-342, Poland

## Supporting Information

**ABSTRACT:** Single-atom catalysts are often considered as the ultimate design principle for supported catalysts, due to their unique geometric and electronic properties and their highly efficient use of precious materials. Here, we report a single-atom catalyst, Cu/Uio-66, prepared by a covalent attachment of Cu atoms to the defect sites at the zirconium oxide clusters of the metal–organic framework (MOF) Uio-66. Kinetic measurements show this catalyst to be highly active and stable under realistic reaction conditions for two important test reactions, the oxidation of CO at temperatures up to 350 °C, which makes this interesting for application in catalytic converters for cars, and for CO removal via selective oxidation of CO in H<sub>2</sub>-rich feed gases, where it shows an excellent selectivity of about 100% for CO oxidation. Time-resolved *operando* spectroscopy measurements indicate that the activity of the catalyst is associated with atomically dispersed, positively charged ionic Cu species. Density functional theory (DFT) calculations in combination with experimental data show that Cu binds to the MOF by –OH/–OH<sub>2</sub> ligands capping the defect sites at the Zr oxide clusters.



## INTRODUCTION

Reduction of the size of metal nanoparticles in supported catalysts to the atomic limits, ultimately arriving at so-called single-atom catalysts, has been a long-standing dream in heterogeneous catalysis, both to maximize the fraction of active sites and increase their selectivity for specific reaction pathways.<sup>1–4</sup> The challenge is, however, to stabilize and prevent the individual metal atoms or small clusters from migrating and sintering during reaction, which is a common cause of catalyst deactivation, especially at high temperatures.<sup>5–7</sup> Extensive efforts to solve this problem have focused on loading minute amounts of active metal onto supports with high surface area such as activated carbon, zeolites, or metal oxides. This approach depends largely on providing sufficiently large spacings between active metal species. However, precise control of the spatial location and the local environment of such metal atoms or small clusters on these mostly ill-defined surface structures remains difficult. We envisaged another approach, using a regularly structured metal–organic framework (MOF) as template, where active metal atoms are attached to specific sites.<sup>8–10</sup> In addition to the well-defined environment of the active metal atoms,<sup>11–14</sup> metal–support interactions may assist also in stabilizing these atoms and thus

hinder sintering.<sup>12,15,16</sup> Although anchoring of metal atoms at metal oxide clusters in MOFs has been reported in a number of studies, these metal atoms sinter under reducing conditions due to the presence of nearby metal atoms or the lack of interaction with MOFs.<sup>10,17–19</sup>

In the present contribution, we report on a single atom Cu/Uio-66 catalyst, where Cu atoms are covalently attached to the defect sites of the Zr oxide clusters in Uio-66, Zr<sub>6</sub>O<sub>4</sub>(OH)<sub>4</sub>(BDC)<sub>5</sub>(CH<sub>3</sub>COO)<sub>0.7</sub>(H<sub>2</sub>O)<sub>1.3</sub>(OH)<sub>1.3</sub> (BDC<sup>2-</sup> = 1,4-benzenedicarboxylate), and the performance of these catalysts in the CO oxidation reaction under completely realistic reaction conditions. This reaction is a key reaction in heterogeneous catalysis, both from a fundamental point of view and for practical applications, e.g., for reducing CO emissions in exhaust gases or for the removal of CO from H<sub>2</sub>-rich feed gases for ammonia synthesis and low temperature fuel cell applications.<sup>20</sup> We used a combination of kinetic studies as well as time-resolved *operando* and *ex situ* spectroscopy together with electron microscopy measurements, and of computational studies, which provided detailed insight into the

Received: October 22, 2018

Published: March 10, 2019

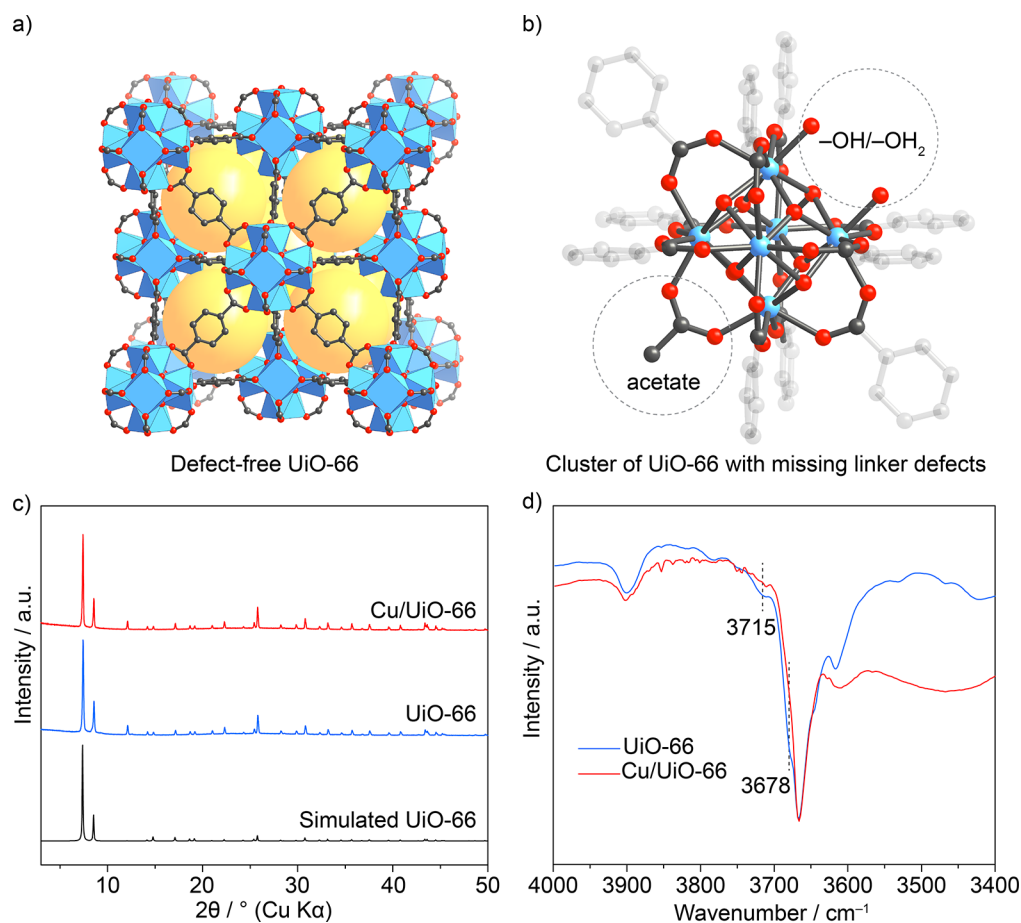


**Figure 1.** (a) Crystal structure of defect-free UiO-66 (yellow spheres represent the space in the framework). (b) Zr oxide cluster of UiO-66 with  $-OH/-OH_2$  and acetate molecules replacing terephthalate linkers. Atom labeling scheme: C: black; O: red; Zr: blue (H atoms are omitted for clarity). (c) Measured PXRD diffractograms of UiO-66 and Cu/UiO-66 in comparison with a simulated diffractogram of UiO-66. (d) DRIFTS spectrum of UiO-66 overlaid with that of Cu/UiO-66.

structure and electronic properties of the catalyst during activation and subsequent reaction, making use also of the well-defined structure of the catalyst.

## EXPERIMENTAL METHODS

**Synthesis of the Catalyst UiO-66.**<sup>15</sup> In a 20 mL scintillation vial, 1,4-benzenedicarboxylic acid (25 mg) and zirconium tetrachloride (33.4 mg) were dissolved in a solution containing DMF (10 mL) and acetic acid (0.7 mL). The vial was sealed and heated isothermally at 120 °C for a day. Subsequently, UiO-66 powder was collected by centrifugation, washed, and dried under dynamic vacuum overnight (further details in the [Supporting Information, Section S1](#)).

**Cu/UiO-66.** UiO-66 (600 mg) was added to the solution containing  $CuCl_2 \cdot 2H_2O$  (Aldrich, 99.99%, 540 mg) dissolved in DMF (9 mL). The suspension was sonicated for 1 min. The vial's thread was wrapped with PTFE tape, and then the vial was sealed and heated in an 85 °C isothermal oven for a day. Finally, the product was collected by centrifugation, washed, and dried under dynamic vacuum overnight (further details in the [Supporting Information, Section S1](#)).

**Activity Measurements.** The kinetic measurements were carried out after pretreatment (10%  $H_2/N_2$  for 1 h at 250 °C) in a quartz tube microreactor (4 mm inner diameter) at atmospheric pressure, where the as-prepared catalyst powder was positioned in the middle of the reactor and fixed on both sides by a piece of quartz wool. All measurements were carried out using high purity gases (99.999%, supplied by Westfalen AG) and Hastings HFC-202 mass flow controllers for preparing gas mixtures. Activity measurements were performed in idealized (1% CO, 1%  $O_2$ ,  $N_2$  balance),  $O_2$ -rich (1% CO, 21%  $O_2$ ,  $N_2$  balance), and  $H_2$ -rich (1% CO, 1%  $O_2$ , 80%  $H_2$ ,  $N_2$

balance) gas mixtures. Evaluation of the Weisz criterion showed the absence of mass-transport related problems.<sup>21</sup> Influent and effluent gases were analyzed by online gas chromatography (GC) with a CO detection limit of <10 ppm (DANI 86.10), using  $H_2$  as a carrier gas. The GC was equipped with two columns packed with Haysep Q polymer for separating CO,  $O_2$ , and  $N_2$  and a molecular sieve (5 Å) for separating  $CO_2$  and  $H_2O$ . For gas composition analysis, two thermal conductivity detectors (TCDs) were used. The Cu mass-normalized reaction rates ( $R_{CO}$ ) were calculated from the CO conversion ( $X_{CO}$ ) under differential reaction conditions ( $X_{CO} < 20\%$ ) in the idealized reaction gas, using the molar flow rate of CO into the reactor ( $n_{CO,in}$ ), and the absolute mass of Cu metal in the catalyst ( $m_{Cu}$ ) according to [eq 1](#). Differential reaction conditions were ensured by diluting the catalyst with  $\alpha-Al_2O_3$ , which is catalytically inactive under these conditions (pure catalyst: 10–120 mg). The selectivity for CO oxidation ( $S$ ) during PROX measurements was obtained from the formation of  $CO_2$  ( $X_{CO_2}$ ) and water ( $X_{H_2O}$ ), according to [eq 2](#). Including the atomic mass of Cu ( $M_{Cu}$ ) and metal dispersion ( $D_{Cu} = 100\%$  considering atomic dispersion) TOF values were obtained according to [eq 3](#).

$$R_{CO} = \frac{\dot{X}_{CO} n_{CO,in}}{m_{Cu}} \quad (1)$$

$$S = \frac{X_{CO_2}}{X_{CO_2} + X_{H_2O}} \times 100 \quad (2)$$

$$\text{TOF}_{\text{CO}} = \frac{R_{\text{CO}} \times M_{\text{Cu}}}{D_{\text{Cu}}} \quad (3)$$

**Operando DRIFTS Measurements.** Time-resolved *operando* DRIFTS measurements were carried out using a commercial reaction cell (Harricks, HV-DR2), in a continuous flow of reaction gases, with the gases flowing through the catalyst bed from top to bottom, similar to the setup used in kinetic measurements. Measurements were performed under differential reaction conditions, following a H<sub>2</sub> pretreatment. The effluent reaction gases were continuously monitored by transmission infrared spectrometry, using an FTIR spectrometer (Alpha Bruker Optics Inc.) coupled with a substrate-integrated hollow waveguide (iHWG).<sup>22</sup> The DRIFTS spectra were recorded using a Magna 6700 spectrometer (Thermo-Fischer), equipped with an MCT narrow-band gap detector.<sup>23</sup> The intensities of different bands were evaluated in Kubelka–Munk units (KMU), which are linearly proportional to the coverage of adsorbed surface species.<sup>24</sup> Background subtraction and normalization of the spectra were performed using spectra recorded in a flow of N<sub>2</sub> directly after the catalyst pretreatment, normalizing to identical intensity at 3855 cm<sup>-1</sup>. For comparison of UiO-66 and Cu/UiO-66, the spectra were normalized at the  $\mu$ -OH vibration of the Zr secondary building unit located at 3666 cm<sup>-1</sup>.

**Operando XAS Measurements.** *Operando* XANES and EXAFS measurements were conducted in transmission mode at the Cu K-edge at the P65 beamline of the PETRA-III extension (DESY) and at the XAFS beamline of the Elettra Synchrotrone. In all experiments, we used a specially designed reaction cell, which was described in detail elsewhere.<sup>25</sup> The measurements were carried out under differential reaction conditions (CO conversion <5%) after identical pretreatment to that described in kinetic measurements using ~20 mg of diluted Cu/UiO-66 under a continuous flow of an idealized CO oxidation gas mixture, where the conversion was recorded using online gas chromatography (influent and effluent gases). Although the much higher space velocity in the XAS measurements led to different reaction rates compared to the kinetic measurements in the microreactor, the trend of catalyst activation agrees well with the respective microreactor data (Supporting Information, Figure S13). Background subtraction and normalization of the XANES spectra were performed using the Athena software from the IFEFFIT program package.<sup>26</sup> Linear combination fitting of the XANES spectra was carried out using reference spectra of Cu foil, CuO, and Cu<sub>2</sub>O. For data reduction and evaluation of the EXAFS spectra we used the XDAP software package with standard procedures described elsewhere.<sup>27,28</sup> Theoretical references were calculated by the FEFF 8.0 code and then calibrated using experimental EXAFS spectra of Cu foil and CuO as well as Cu<sub>2</sub>O powder as experimental references.<sup>27,29</sup> EXAFS data were evaluated in R-space using fixed *k* and *R* ranges (*k*: 2.8–9.5 Å<sup>-1</sup>; *R*: 0.0–5.0 Å). The data were fitted to the shortest backscatterer distance around the Cu absorber (i.e., first Cu–Cu, Cu–Zr, and Cu–O shell); the bond length, coordination number (CN), internal energy shift (*E*<sub>0</sub>), and Debye–Waller factor (DFW) were allowed to change freely (resulting values ranged from 0.003 to 0.004 Å<sup>2</sup>).

**Electron Microscopy.** High-angle annular dark-field scanning transmission electron microscopy (HAADF-STEM) measurements were performed on a Cs-corrected FEI Titan electron microscope operated at 300 keV. Energy dispersive spectroscopy (EDS) mapping was carried out on a Talos F200 FEI TEM microscope operated at 200 keV, which is equipped with a FEG cathode and the Super EDS system. The sample was dispersed in ethanol and dip-coated on a carbon coated Ni grid.

**X-ray Photoelectron Spectroscopy (XPS).** XPS measurements were carried out on a PHI 5800 ESCA system (Physical Electronics) using monochromatic Al–K<sub>α</sub> radiation (1486 eV) and an electron emission angle of 45°. Pass energies were 93.9 eV for survey spectra and 29.35 eV for high-resolution spectra. XPSPEAK4.1 software was used to deconvolute the measured signals, employing a Shirley background correction and Gaussian/Lorentzian peak shapes. The

binding energies (BEs) of all spectra were calibrated by C(1s) peak of ubiquitous carbon at 284.8 eV.

## RESULTS AND DISCUSSION

**Synthesis of Cu/UiO-66 Catalyst.** We synthesized UiO-66 using acetic acid as a modulator to control the particle size and obtain highly crystalline MOF (Figure 1a). As commonly observed, the MOF prepared here contains missing linkers, resulting in defect sites on the Zr oxide cluster.<sup>30–33</sup> From <sup>1</sup>H nuclear magnetic resonance (NMR) analysis, elemental analysis, and thermal gravimetric analysis (Supporting Information, Figures S1–S3), we found that the MOF contains about one missing linker per one Zr<sub>6</sub> cluster and that the resulting defect sites are terminated by acetate and –OH/–OH<sub>2</sub> groups. This yields Zr<sub>6</sub>O<sub>4</sub>(OH)<sub>4</sub>(C<sub>8</sub>H<sub>4</sub>O<sub>4</sub>)<sub>5</sub>–(CH<sub>3</sub>COO)<sub>0.7</sub>(H<sub>2</sub>O)<sub>1.3</sub>(OH)<sub>1.3</sub> as the actual chemical composition of the UiO-66 material synthesized here (Figure 1b). Cu/UiO-66 catalyst was prepared by heating UiO-66 in a solution of CuCl<sub>2</sub>·2H<sub>2</sub>O in DMF at 85 °C overnight to anchor Cu atoms at the oxygen atoms of –OH/–OH<sub>2</sub> groups terminating the defect sites. Inductively coupled plasma optical emission spectroscopy (ICP-OES) analysis of Cu/UiO-66 shows the incorporation of Cu in Cu/UiO-66 with a Cu:Zr<sub>6</sub> atomic ratio of 0.8. Independent of the excess of CuCl<sub>2</sub>·2H<sub>2</sub>O used in the synthesis, this ratio remained constant, indicating that the defect sites of the UiO-66 are the limiting feature. Scanning electron microscopy (SEM) images of the materials before and after the loading of Cu show the typical octahedral morphology of UiO-66 crystals without any impurity phase (Supporting Information, Figure S4). Energy dispersive X-ray spectroscopic (EDS) analysis indicates the presence of Cl, with a molar ratio of Cu:Cl of about 1, suggesting that Cl<sup>-</sup> may function as a ligand coordinating to Cu (Supporting Information, Figure S5). From transmission electron microscopy (TEM) images of the fresh Cu/UiO-66 (Supporting Information, Figure S6a), we did not find any evidence for Cu or CuO<sub>x</sub> nanoparticle formation. Powder X-ray diffraction (PXRD) of Cu/UiO-66 displays the reflections expected from simulation of UiO-66, supporting the phase purity of UiO-66 (Figure 1c). Diffuse reflectance FTIR spectroscopy (DRIFTS) spectra of Cu/UiO-66 obtained under a continuous flow of N<sub>2</sub> at 250 °C show a significantly lower intensity of the bands at 3715 and 3678 cm<sup>-1</sup> compared to that observed for UiO-66, which are attributed to the O–H stretch vibrations of the defect sites on the Zr oxide clusters (Figure 1d). This can be explained by a mechanism, where Cu atoms are coordinating to –OH/–OH<sub>2</sub> species on UiO-66.

To gain more information on the structure of the catalyst, we prepared single crystals of Cu/UiO-66, following a similar metalation procedure as used for the microcrystalline Cu/UiO-66 sample. Single crystal X-ray diffraction (SCXRD) analysis reveals that Cu/UiO-66 crystallizes in the *Fm*–*3m* space group with a structure similar to the native UiO-66 (Supporting Information, Section S2.5; Figure S7 and Figure S8), indicating that the framework remains unperturbed upon Cu metalation. However, the disorder and the low concentration of the dispersed Cu atoms did not allow for an unambiguous identification of the Cu configuration by SCXRD (see Supporting Information, section S2.5).

Therefore, we performed *operando* X-ray absorption spectroscopy (XAS) measurements of the Cu/UiO-66 catalyst to obtain further information on the structure of the Cu site, which will be discussed further below.

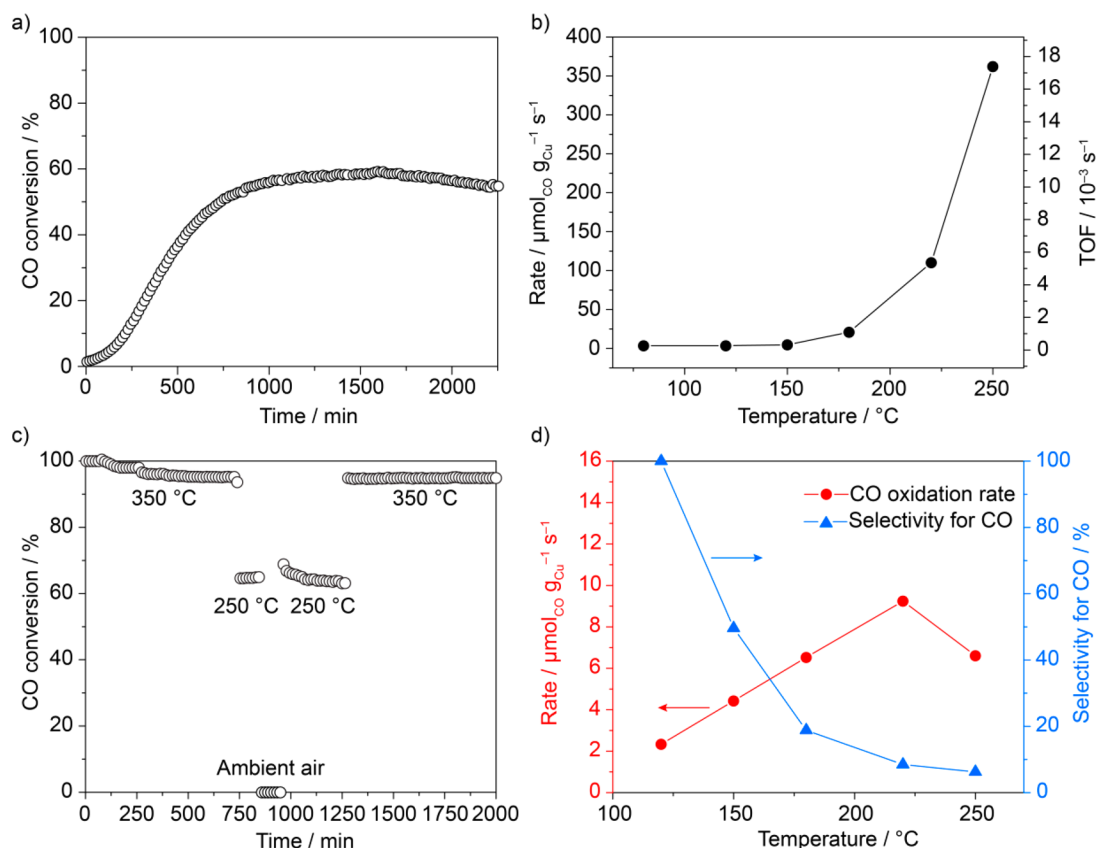


**Figure 2.** (a) CO oxidation during time on stream based on the CO conversion signal at 250 °C on 120 mg of the catalyst (1:4 dilution) after pretreatment (10% H<sub>2</sub>/N<sub>2</sub> for 1 h at 250 °C) in an idealized reaction gas mixture (1% CO, 1% O<sub>2</sub>, N<sub>2</sub> balance – 30 NmL min<sup>-1</sup>). (b) Temperature dependence of the reaction rates and turnover frequencies (TOFs) between 80 and 250 °C after reaching steady state at 250 °C in an idealized reaction gas mixture. (c) CO conversion in synthetic air (1% CO, 21% O<sub>2</sub>, balance N<sub>2</sub> – 30 NmL min<sup>-1</sup>) at different temperatures and upon shutdown of the reaction (cooling from 250 to 25 °C and kept in air at 25 °C for 2 h) and restart by heating in a reaction gas mixture to 250 °C and subsequently to 350 °C. (d) Cu mass normalized CO oxidation rates at different temperatures (120–250 °C) as determined in a measurement at different temperatures in a H<sub>2</sub>-rich preferential CO oxidation gas mixture (1% CO, 1% O<sub>2</sub>, 80% H<sub>2</sub>, N<sub>2</sub> balance – 30 NmL min<sup>-1</sup>) and catalyst selectivity for CO oxidation (see details in ‘Methods’ section).

**CO Oxidation and Preferential CO Oxidation.** Before reaction, we pretreated Cu/Uio-66 catalyst in 10% H<sub>2</sub>/N<sub>2</sub> at 250 °C for 1 h. Subsequently, the catalytic activity for CO oxidation was measured in an idealized gas mixture (1% CO, 1% O<sub>2</sub>, N<sub>2</sub> balance) at 250 °C for almost 37.5 h (Figure 2a). The catalyst first passed through a pronounced activation phase, which lasted over 12.5 h, followed by a slowly increasing activity, until it reached its highest activity at about 57% conversion after ~25 h on stream. Afterward the activity decayed slightly, losing about 2% conversion up to 37.5 h on stream. We also examined the temperature-dependence of the catalytic activity between 80 and 250 °C under differential reaction conditions, using appropriate amounts of catalyst at each temperature. As depicted in Figure 2b, the Cu mass normalized activity and the corresponding turnover frequencies (TOFs) display an essentially exponential dependence on the reaction temperature, which reflects an apparent activation energy of  $43.5 \pm 2$  kJ mol<sup>-1</sup>. Assuming that all Cu atoms are accessible to the reactants, TOF values were determined to be between  $0.22 \times 10^{-3}$  s<sup>-1</sup> at 80 °C and  $17.5 \times 10^{-3}$  s<sup>-1</sup> at 250 °C (Figure 2b). Considering a possible application in catalytic converters in cars, where 350 °C is a typical reaction temperature under high load conditions,<sup>34</sup> we tested the catalyst performance at 350 °C under otherwise identical conditions. Over more than 20 h we did not find any

measurable decay in reaction rate (Supporting Information, Figure S9).

Finally, we evaluated the influence of excess oxygen on the catalyst performance under these conditions, reacting 1% CO in synthetic air (21% O<sub>2</sub>, 78% N<sub>2</sub>) at 350 °C (Figure 2c). Under these conditions, the catalyst shows a CO conversion of 98% for over 700 min. Upon reducing the temperature to 250 °C, the CO conversion decayed to ~65%. To further test the response of the catalyst to dynamic variations of the load, in this case to complete shutdown of the engine, we removed CO from the gas feed and abruptly decreased the temperature to 25 °C under a continuous flow of synthetic air for 2 h. Afterward, the original feed gas was reconnected, and the temperature was increased to 250 °C within 5 min. After a short period of time, where an overshoot in temperature caused a slightly higher CO conversion, we arrived at essentially the same CO conversion as before the shutdown procedure. Further increasing the reaction temperature to 350 °C also led to about the same conversion of 98%, identical to the original value before the shutdown step. Hence, the shutdown procedure did not cause any measurable irreversible loss in activity. Comparing the CO oxidation activity of Cu/Uio-66 under these conditions to that of Cu/CeO<sub>2</sub> and Cu/ZrO<sub>2</sub>, which are among the most active Cu-based catalysts for CO oxidation, Cu/Uio-66 catalyst is at least 3 times more

active based on the CO conversion for similar Cu masses.<sup>35,36</sup> Compared to Pt/CeO<sub>2</sub> catalysts, for the same metal loading, the activity is in the same order of magnitude at temperatures around 200 °C.<sup>37</sup>

As a second example, we evaluated the catalyst performance for the preferential oxidation of CO (PROX) in a H<sub>2</sub>-rich reformat gas (1% CO, 1% O<sub>2</sub>, 18% N<sub>2</sub>, and 80% H<sub>2</sub>) (Figure 2d), where CO should be completely removed, while the competing oxidation of H<sub>2</sub> should be kept as low as possible. At 120 °C, the catalyst showed no measurable activity for H<sub>2</sub> oxidation (Supporting Information, Figure S10), while the CO oxidation activity is around 2.3 μmol g<sub>Cu</sub><sup>-1</sup> s<sup>-1</sup>, which is slightly lower than in the absence of H<sub>2</sub> (3.5 μmol g<sub>Cu</sub><sup>-1</sup> s<sup>-1</sup>) under otherwise identical reaction conditions. This is different from the behavior of supported Au and Pt catalysts, where the presence of H<sub>2</sub> tended to increase the CO oxidation rate.<sup>38,39</sup> This results in a selectivity for CO oxidation of about 100%. In contrast to the CO oxidation in H<sub>2</sub>-free reaction gas (Figure 2b), the CO oxidation rate increased about linearly with increasing temperature in the H<sub>2</sub>-rich gas mixture up to 220 °C (Figure 2d) and then decayed onward to 250 °C. The selectivity for CO oxidation, on the other hand, decreased with increasing temperature. Considering the constant H<sub>2</sub> conversion between 220 and 250 °C (Supporting Information, Figure S10), the decay in CO rate at 250 °C most likely results from the increasing competition for O<sub>2</sub> due to the high H<sub>2</sub> oxidation rate. This conclusion of about 100% selectivity was confirmed by an additional measurement at higher CO conversion (ca. 5%), which also revealed a selectivity toward CO oxidation of about 100% (error: ±1.5%) over 950 min (Supporting Information, Figure S10).

After the reaction, we examined the structural integrity of the catalyst using a combination of PXRD, TEM, and DRIFTS measurements. The comparison of the PXRD patterns of the fresh and the spent Cu/Uio-66 catalysts (Figure 1 and Supporting Information, Figure S11), after the exposure to the reaction as described with Figure 2c, indicates that the phase purity and crystallinity of the catalyst are retained, underlining the high stability of the catalyst. Furthermore, bright field TEM images show no significant changes in the shape and size distribution of the MOF crystals after CO oxidation, based on an evaluation of over 600 crystals. In both cases neither Cu nor Cu oxide clusters could be detected (Supporting Information, Figure S6). The stability of the organic component of the catalyst was investigated by DRIFTS measurements. Measurements performed after different activation and reaction steps showed no measurable differences in the IR spectra, further supporting the high stability of the Cu/Uio-66 catalyst during the reaction (Supporting Information, Figure S12).

**Adsorption of CO during the Reaction.** Time-resolved *operando* DRIFTS measurements were performed during CO oxidation at 250 °C under a continuous flow of the idealized reaction gas mixture. Sequences of DRIFTS spectra are shown in Figure 3. The upper panel covers the initial phase of the reaction, ranging from 0 to 30 min, and the lower one provides long-term information extending from 30 to 1500 min. Both panels show the evolution of the CO<sub>2</sub> gas phase signal with bands at 2332 and 2362 cm<sup>-1</sup>, whose intensity follows the trend of the CO oxidation rate with time (see the Supporting Information, Figure S13a for integrated intensity). During the initial 20 min, we found a distinct CO adsorption band at 2113 cm<sup>-1</sup>, which is near the position of CO adsorbed on oxidized Cu nanoparticles (Cu<sup>1+</sup>-monocarbonyl species) at around

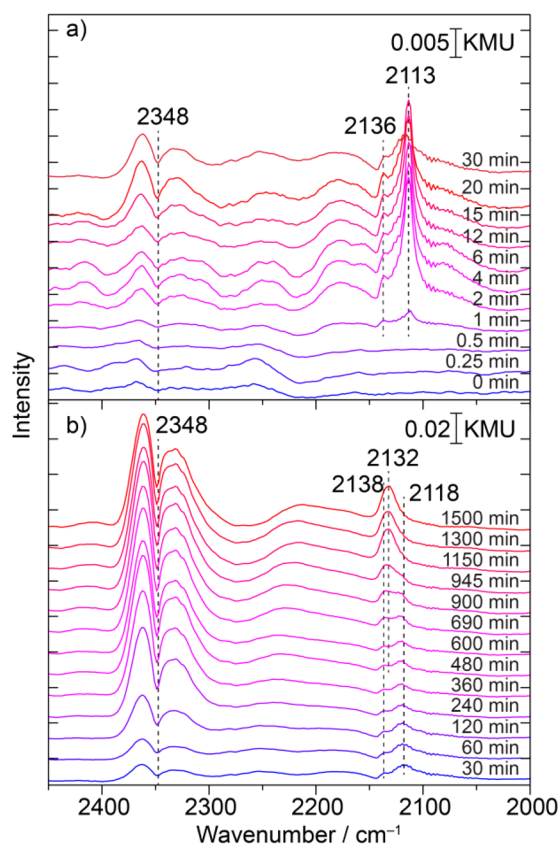


**Figure 3.** Selected DRIFTS spectra of CO adsorption and CO<sub>2</sub> formation recorded during the first 20 min (a) and at extended reaction times from 30 to 1500 min (b) during CO oxidation in an idealized CO oxidation gas mixture (1% CO, 1% O<sub>2</sub>, N<sub>2</sub> balance – 30 NmL min<sup>-1</sup>, T = 250 °C).

2130 cm<sup>-1</sup> (Figure 3a),<sup>40,41</sup> suggesting the different environment of the covalently bound Cu species in the present case. This band starts to decrease in intensity after 20 min and decays to about 30% of its maximum intensity after 30 min in total. The same band is accompanied by a smaller shoulder at 2138 cm<sup>-1</sup>, which remains, however, rather weak and does not grow with time (Figure 3b). For longer reaction times, starting at about 600 min, a broader band centered around 2132 cm<sup>-1</sup> developed and grew, which is characteristic for a Cu<sup>1+</sup>-monocarbonyl species.<sup>40,41</sup> This band remains stable for reaction times over 1200 min (Supporting Information, Figure S13b). In these assignments it has to be considered, however, that the wavenumber regions reported for Cu<sup>1+</sup> mono- and multicarbonyls varied widely in previous studies.<sup>42</sup> On the other hand, Cu<sup>2+</sup>-CO species were generally considered to be weakly bound and observed only at below ambient temperature.<sup>42</sup> Altogether, these results indicate that there are significant changes in the adlayer and presumably also in the catalyst structure and electronic properties of the Cu species, once at 0 min and ~20 min on stream and once again after 600 min on stream. The former is most likely associated with an initial activation, which will be discussed in more detail after presenting the *operando* XAS data.

**Geometric and Electronic Properties of the Cu Site during the Reactions.** To further identify possible changes in the electronic properties and in the local coordination environment of the Cu species during the CO oxidation reaction, we performed time-resolved *operando* XAS measure-

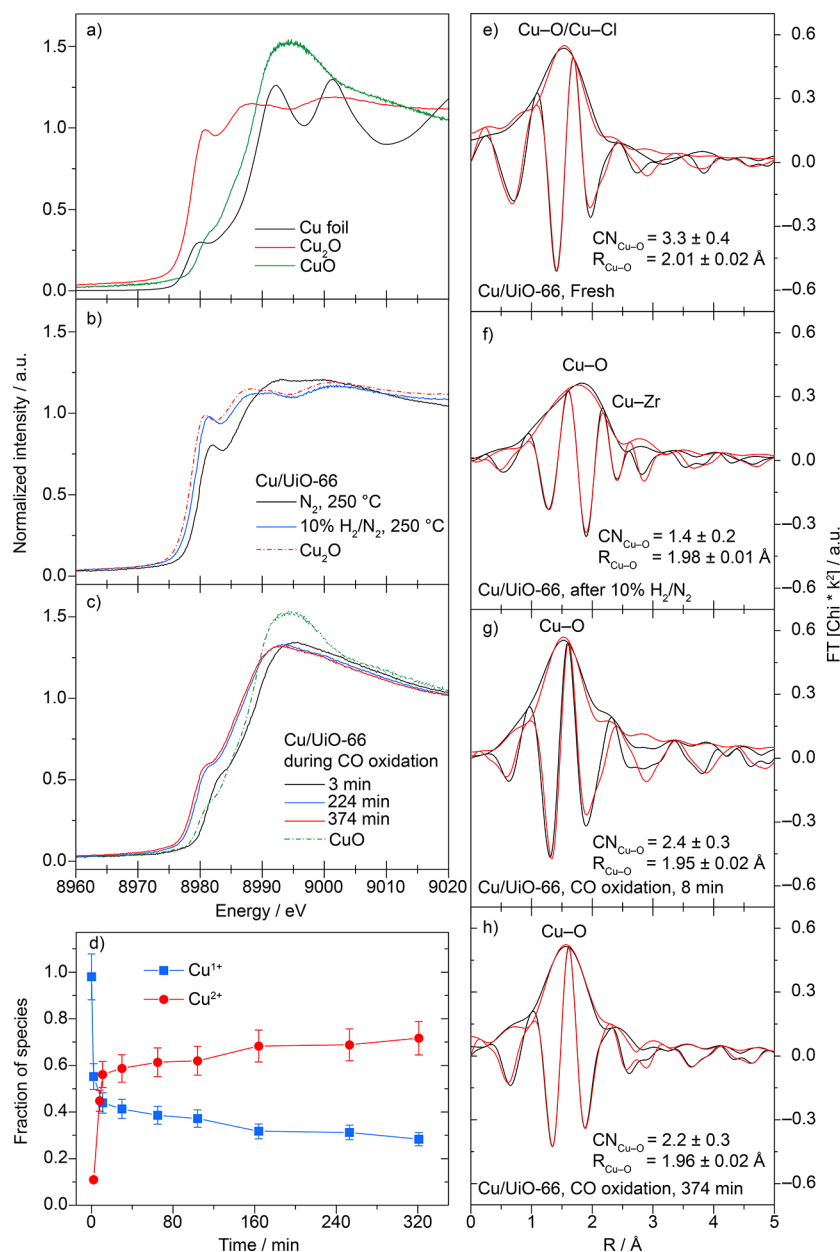


**Figure 4.** (a) Standard XANES spectra of a Cu foil,  $\text{Cu}_2\text{O}$ , and  $\text{CuO}$  recorded as references in  $\text{N}_2$  at  $250^\circ\text{C}$ . (b) Normalized XANES spectra of  $\text{Cu}/\text{UiO}-66$  recorded after drying in  $\text{N}_2$  at  $250^\circ\text{C}$  and after subsequent pretreatment in  $10\% \text{H}_2/\text{N}_2$ , overlaid with a XANES spectrum of  $\text{Cu}_2\text{O}$ . (c) Normalized XANES spectra of  $\text{Cu}/\text{UiO}-66$  recorded during CO oxidation in an idealized CO oxidation gas mixture ( $1\% \text{CO}$ ,  $1\% \text{O}_2$ ,  $\text{N}_2$  balance –  $30 \text{ NmL min}^{-1}$ ) at selected times during the reaction, overlaid with a XANES spectrum of  $\text{CuO}$ . (d) Linear combination analysis (LCA) of the XANES spectra recorded during CO oxidation based on the reference spectra presented in a). (e, f, g, h) Fourier transformed EXAFS spectra of the fresh  $\text{Cu}/\text{UiO}-66$  catalyst in  $\text{N}_2$  at  $25^\circ\text{C}$  (e), the catalyst in  $\text{N}_2$  after pretreatment in  $10\% \text{H}_2/\text{N}_2$  (f), during CO oxidation in an idealized reaction gas mixture after 8 min (g) and after 374 min on stream (h).

ments at the Cu K-edge (Figure 4) under a continuous flow of reaction gas (Supporting Information, Figure S14). In the near-edge region (Figure 4b), X-ray absorption near-edge structure (XANES) spectra show a significant reduction of the white line intensity located at  $\sim 8982 \text{ eV}$  after the hydrogen pretreatment of  $\text{Cu}/\text{UiO}-66$  at  $250^\circ\text{C}$ , pointing to a reduction of the initial  $\text{Cu}^{2+}$  species. Comparison with the reference XANES spectra of  $\text{Cu}$ ,  $\text{Cu}_2\text{O}$ , and  $\text{CuO}$  (Figure 4a)<sup>43–45</sup> shows that this corresponds to a change in the oxidation state of the majority of Cu species from  $\text{Cu}^{2+}$  to  $\text{Cu}^{1+}$ , although there are still differences in details between spectra of the reduced  $\text{Cu}/\text{UiO}-66$  catalyst and  $\text{Cu}_2\text{O}$ , e.g., in the onset

behavior or in the exact position of the white line (see the dashed line in Figure 4b and Figure S15 in the Supporting Information). These differences, which are well outside the error range, point to distinct differences in the chemical environment of the  $\text{Cu}^{1+}$  in the reduced  $\text{Cu}/\text{UiO}-66$  catalyst and in the  $\text{Cu}_2\text{O}$  reference. This will be discussed further with the EXAFS data presented below. In contrast to Cu species supported on NU-1000, a Zr-based MOF, where  $\text{Cu}^{2+}$  were readily reduced and sintered to  $\text{Cu}^0$  under similar reduction conditions,  $\text{Cu}^{2+}$  species in  $\text{Cu}/\text{UiO}-66$  are resistant toward complete reduction to  $\text{Cu}^0$ , signifying the stability of this single-site catalyst, likely imposed by the presence of a single

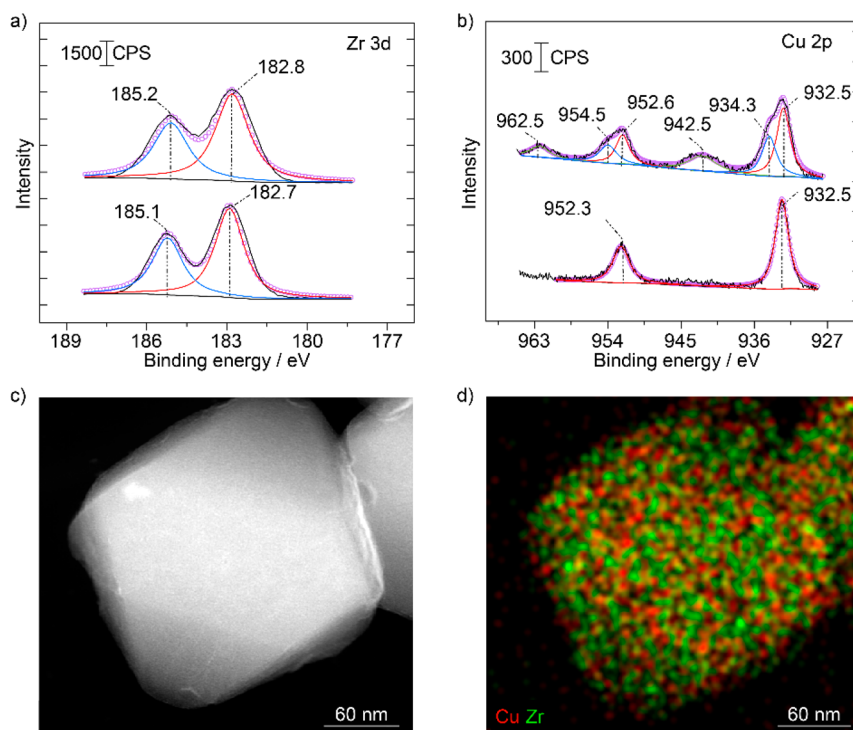


**Figure 5.** X-ray photoelectron spectroscopy spectra of Cu/Uio-66 in (a) the Zr 3d region and (b) the Cu 2p region recorded after H<sub>2</sub> treatment (bottom spectra) and after CO oxidation (see text, upper spectra). (c) High-angle annular dark-field scanning transmission electron microscopy (HAADF-STEM) image of the Cu/Uio-66 catalyst after CO oxidation during a temperature scan from 80 to 350 °C and (d) the corresponding EDS map of the Cu and Zr K<sub>α</sub> lines.

Cu atom per Zr cluster. For quantitative information we performed a linear combination analysis (LCA) of the XANES spectra in Figure 4d. This confirms that an oxidation state of 1+ is obtained for all Cu species after the H<sub>2</sub> pretreatment. After changing to the reaction gas mixture, 55–60% of the initial Cu<sup>1+</sup> species in the Cu/Uio-66 catalyst were oxidized to Cu<sup>2+</sup> within 3 min on stream (Figure 4c), and this trend slowly continued; thus the local –HO–Cu–OH– coordinations were increasingly converted to –O–Cu–O– or to –O–Cu–OH like coordinations, as indicated by the shift of the edge jump to higher energy from the initial spectra to later ones (Figure 4c).<sup>46</sup>

Eventually, a composition of 70% Cu<sup>2+</sup> and 30% Cu<sup>1+</sup> was reached after 375 min on stream. It should be noted that based on the data we cannot distinguish between a mixture of 70% Cu<sup>2+</sup> and 30% Cu<sup>1+</sup> and a situation with 100% of a Cu<sup>1.7+</sup> species, where the lower charge (compared to Cu<sup>2+</sup>) is due to a covalent bond contribution.<sup>47</sup> The fast change in the oxidation state of the Cu species during CO oxidation, from 1+ to a higher oxidation state, agrees well with the fast decay in the intensity of the monocarbonyls adsorbed on Cu<sup>1+</sup> sites (2113 cm<sup>-1</sup>) observed in the DRIFTS measurements. The higher wavenumber band developing after about 600 min of CO oxidation at 2132 cm<sup>-1</sup> indicates a change in the nature of the Cu<sup>1+</sup> formed during reaction, which might indicate a possible restructuring of the binding configuration of these species after longer reaction times. It should also be noted that since we essentially only see Cu<sup>1+</sup>-CO species in the IR spectra, these are the active sites for the reaction. The absence of a visible band for Cu<sup>2+</sup>-CO moieties mainly reflects the much lower stability of these species and hence their lower abundance during reaction. Nevertheless, they may be involved in the reaction process, leaving the question for the active Cu species

open. To test for thermal effects on the stability of the Cu<sup>2+</sup> species under reaction conditions, we carried out similar XANES measurements during CO oxidation (1% CO, 1% O<sub>2</sub>, N<sub>2</sub> balance) at higher temperature, at 350 °C. Despite the high temperature, the LCA of the XANES spectra showed 75% CuO and 25% Cu<sub>2</sub>O, only slightly above the values obtained at 250 °C (Supporting Information, Figure S16). Analysis of the extended X-ray absorption fine structure (EXAFS) spectra recorded during pretreatment and CO oxidation at 250 °C under similar conditions (Supporting Information, Figure S17) provided further information on the local environment of the Cu species during reaction. The Fourier transformed spectrum of the fresh Cu/Uio-66 catalyst shown in Figure 4e reflects a distance of the main backscattering shell of 2.01 ± 0.02 Å. This is assigned to a Cu–O shell with an average coordination number of 3.3 ± 0.4. This indicates that Cu is bound to the Zr oxide clusters of Uio-66 via the oxygen atoms,<sup>43,45</sup> confirming our conclusions based on the DRIFTS and XANES data in Figures 1d and 4a–d described above. After the H<sub>2</sub> pretreatment, the main backscattering of Cu–O was observed at 1.98 ± 0.02 Å with a significant decrease of the coordination number to 1.4 ± 0.2 (Figure 4f). This bond length is significantly longer than Cu–O bonds in Cu<sub>2</sub>O (1.85 Å), providing further proof of distinct differences in the coordination environments of the Cu atoms in Cu/Uio-66 and in Cu<sub>2</sub>O (Supporting Information, Figure S18). Interestingly, we also find a contribution, which would be equivalent to 2.88 ± 0.02 Å for Cu–Cu backscattering, which is, however, significantly larger than a typical Cu–Cu shell in metallic Cu and shorter than in Cu oxides. As one possibility, this contribution may be related to Cu–Zr backscattering.<sup>44,45</sup> After 8 min of CO oxidation, this shell disappeared (Figures 4g–h), while the Cu–O shell at 1.95 ± 0.02 Å remained stable

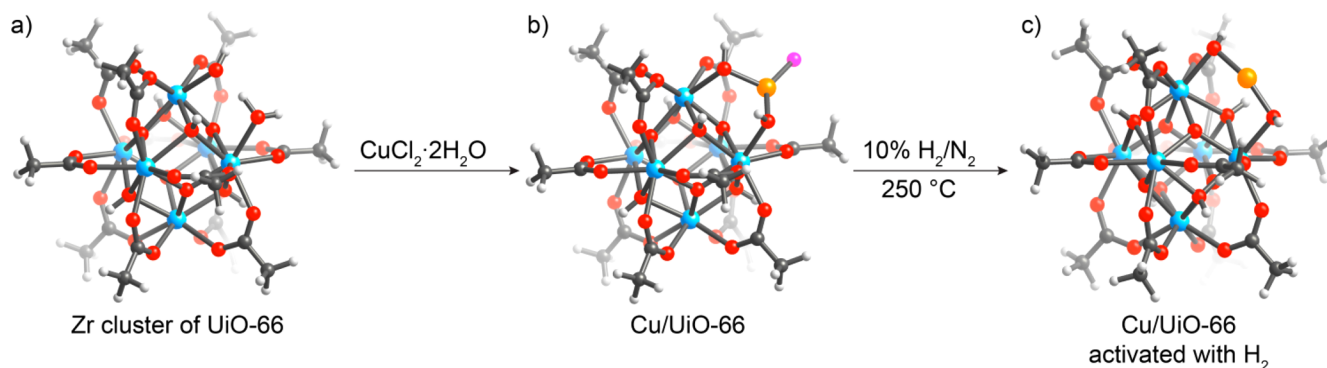


**Figure 6.** DFT calculated structures (a) of defective UiO-66, (b) of a Cu/UiO-66 catalyst where Cu is coordinated to a  $-\text{OH}/-\text{OH}_2$  defect site of UiO-66, and (c) of a Cu/UiO-66 catalyst after activation with H<sub>2</sub>. Atom labeling: C: black; O: red; Cl: pink; Cu: orange; Zr: blue. H: light gray.

during reaction, also at longer reaction times up to 374 min (Figures 4h), but with a higher coordination number of  $2.3 \pm 0.3$ .

Overall, comparison of the EXAFS data collected over a time of 375 min showed little change in both Cu–O distance and coordination number of the Cu species during CO oxidation, except for the changes in the initial few minutes of the reaction (Supporting Information, Figure S19). Also these results point to a high stability of the coordination environment around the Cu atoms during the CO oxidation reaction (see Figure 4h). Altogether, these data underline the presence of individual Cu atoms in an atomically dispersed form, which are coordinated to two oxygen atoms each. This is distinctly different from the situation in Cu<sub>2</sub>O or CuO clusters/nanoparticles.

To gain further information on the chemical state of the Cu species, we analyzed the fresh and spent Cu/UiO-66 catalysts by X-ray photoelectron spectroscopy (XPS). XPS spectra recorded in the Zr 3d region (see Figure 5a) showed insignificant changes of the Zr 3d core level for the spent catalyst ( $3d_{5/2} = 182.7 \pm 0.1$  eV) compared to the fresh, nontreated sample ( $3d_{5/2} = 182.8 \pm 0.1$  eV). These binding energies are characteristic of Zr<sup>4+</sup> ions.<sup>15</sup> For the Cu 2p<sub>3/2</sub> main peak, the core 2p level energy shifts from 932.4 eV for the freshly reduced sample, after H<sub>2</sub> treatment, to 932.7 eV for the spent sample, after CO oxidation at temperatures from 80 to 350 °C (3000 min) (Figure 5b). Additionally, we observed new features at  $942.5 \pm 0.1$  eV (2p<sub>3/2</sub>) and  $962.5 \pm 0.1$  (2p<sub>1/2</sub>) eV after CO oxidation, which are identified as Cu 2p satellites that are characteristic of Cu<sup>2+</sup> ions.<sup>48–50</sup> These satellites have been assigned to a parallel excitation (shakeup) of a ligand electron into an empty Cu 3d state, which do not exist for Cu<sup>1+</sup> and Cu<sup>0</sup>. The absence of the Cu 2p satellite clearly indicates that after H<sub>2</sub> treatment there are only Cu<sup>1+</sup> species present, in full agreement with XANES and EXAFS data. After CO oxidation, the presence of a pronounced Cu 2p satellite demonstrates the formation of Cu<sup>2+</sup> ions. Since the intensity ratio between Cu 2p main peak and the satellite depends on the local environment of the Cu<sup>2+</sup> ions, we cannot determine the Cu<sup>2+</sup>:Cu<sup>1+</sup> ratio from these data. Similar to XANES analysis, a single Cu ion species with a formal charge of about 1.7+ would also be possible.

To further test for the presence of Cu clusters, we performed high-angle annular dark-field scanning transmission electron microscopy (HAADF-STEM) and EDS measurements on the fresh (Supporting Information, Figure S20) and on the spent Cu/UiO-66 catalyst (see Figure 5c, d). For both samples, high resolution HAADF-STEM images do not show any features

indicative of the formation of clusters of Cu, Cu<sub>2</sub>O, or CuO, consistent with our findings from EXAFS. The EDS mapping of over 60 MOF crystals of the fresh and spent samples confirmed that the Cu species are uniformly distributed inside the MOF crystals (Figure 5d), as would be expected for a MOF with single Cu atom. Furthermore, atomic resolution HAADF-STEM images (Supporting Information Figure S21), collected at the outermost parts of MOF microcrystals, show individual atoms/ions, in full agreement with the findings from XANES, EXAFS, and XRD data.

**Density Functional Theory Calculations.** Finally, to obtain more detailed information about the structure of the catalyst, we performed density functional theory (DFT) calculations. Based on the experimental findings, we modeled the Cu/UiO-66 catalyst by anchoring Cu at  $-\text{OH}/-\text{OH}_2$  ligands capping the defect sites of UiO-66 with a Cl<sup>−</sup> as a ligand (Figure 6a). The resulting optimized structure shows that in the fresh sample the Cu ions are 3-fold coordinated, binding to two oxygen atoms and one chlorine atom at bond distances of Cu–O = 1.89 and 1.95 Å and Cu–Cl = 2.15 Å (Figure 6b). To describe the structure after H<sub>2</sub> pretreatment (Figure 6c), where according to the XAS data the Cu species are reduced to Cu<sup>1+</sup> and that these are atomically dispersed, we assumed that Cu is 2-fold coordinated, binding to  $-\text{OH}/-\text{OH}_2$  on the Zr oxide cluster, and that the Cl ligand is removed. The optimized structure of Cu/UiO-66 shows similar Cu–O bond distances of 1.86 Å, in good agreement with the EXAFS results. The decrease of the (formal) Cu–O coordination number during the reductive pretreatment deduced from the EXAFS data points to some loss in the coordination shell, which was not considered in the calculations. Overall, the DFT calculations fully support our structural conclusions derived from the EXAFS measurements.

## CONCLUSIONS

We have prepared a single-atom catalyst, where single Cu atoms are anchored to the oxygen atoms of  $-\text{OH}/-\text{OH}_2$  species capping the defect sites on the Zr oxide clusters of UiO-66. Using the CO oxidation reaction and selective CO oxidation in H<sub>2</sub>-rich feed gases (H<sub>2</sub> purification) as test reactions, we found this catalyst to be highly active and stable even in O<sub>2</sub>-rich reaction atmospheres, under variable load conditions (startup/shutdown operation) and at temperatures up to 350 °C. In addition, it is highly selective (100%) for CO oxidation in the presence of up to 80% H<sub>2</sub> in the gas feed. Time-resolved *operando* spectroscopy indicates that the activity of the catalyst is associated with the atomically dispersed

positively charged Cu species. We anticipate that the strategy reported here can be employed to synthesize single atom catalysts hosting other elements for a broad scope of catalytic transformations. Furthermore, the well-defined active site of this catalyst will enable detailed mechanistic investigations.

## ■ ASSOCIATED CONTENT

### 📄 Supporting Information

The Supporting Information is available free of charge on the ACS Publications website at DOI: 10.1021/jacs.8b11386.

Detailed description of synthesis and characterizations with additional data including BET-isotherms, NMR, TGA, PXRD, SEM, HR-TEM, STEM-EDS, FTIR, XANES, EXAFS, and kinetic measurements (Figures S1–S18) (PDF)

## ■ AUTHOR INFORMATION

### Corresponding Authors

\*juergen.behm@uni-ulm.de

\*yaghi@berkeley.edu

### ORCID

Omar M. Yaghi: 0000-0002-5611-3325

R. Jürgen Behm: 0000-0002-7565-0628

### Author Contributions

#A.M.A.-M. and B.R. contributed equally.

### Notes

The authors declare no competing financial interest.

## ■ ACKNOWLEDGMENTS

B.R. is supported by the Royal Thai Government Scholarship. The research performed in the O.M.Y. laboratory was supported by BASF SE (Ludwigshafen, Germany) and King Abdul-Aziz City for Science and Technology. Research work at the Molecular Foundry was supported by the Office of Science, Office of Basic Energy Sciences, of the DOE under Contract No. DE-AC02-05CH11231. The Molecular Graphics and Computation Facility is funded by the NIH (S10OD023532). The AVB-400 NMR spectrometer is partially supported by NSF Grant CHE-0130862. We thank the Institute of Engineering Materials and Biomaterials of the Silesian University of Technology for access to STEM imaging and the Biological and Chemical Research Centre, University of Warsaw, for the possibility to perform the EDS analysis (cofunded by the European Union/European Regional Development Fund under the Operational Program Innovative Economy, 2007-2013). XAS measurements were carried out at P65 beamline, Petra-III (DESY, Germany) and XAFS beamline in Elettra Synchrotrone (Trieste, Italy). Work at the Advanced Light Source (ALS) is supported by Office of Basic Energy Sciences of the U.S. Department of Energy (DE-AC02-05CH11231). Finally we would like to thank Dr. Thomas Diemant for XPS measurements (Institute of Surface Chemistry and Catalysis, Ulm University) and Drs. Simon J. Teat and Laura J. McCormick for synchrotron X-ray diffraction data acquisition support, and Dr. R. Matheu for assistance with physical characterizations.

## ■ REFERENCES

(1) Qiao, B.; Wang, A.; Yang, X.; Allard, L. F.; Jiang, Z.; Cui, Y.; Liu, J.; Li, J.; Zhang, T. Single-Atom Catalysis of CO Oxidation Using Pt<sub>1</sub>/FeO<sub>x</sub>. *Nat. Chem.* **2011**, *3*, 634–641.

(2) Yang, M.; Li, S.; Wang, Y.; Herron, J. A.; Xu, Y.; Allard, L. F.; Lee, S.; Huang, J.; Mavrikakis, M.; Flytzani-Stephanopoulos, M. Catalytically Active Au-O (OH)<sub>2</sub>-Species Stabilized by Alkali Ions on Zeolites and Mesoporous Oxides. *Science* **2014**, *346*, 1498–1501.

(3) Malta, G.; Kondrat, S. A.; Freakley, S. J.; Davies, C. J.; Lu, L.; Dawson, S.; Thetford, A.; Gibson, E. K.; Morgan, D. J.; Jones, W.; Wells, P. P.; Johnston, P.; Catlow, C. R. A.; Kiely, C. J.; Hutchings, G. J. Identification of Single-Site Gold Catalysis in Acetylene Hydrochlorination. *Science* **2017**, *355*, 1399–1403.

(4) Zhang, H.; Liu, G.; Shi, L.; Ye, J. Single-Atom Catalysts: Emerging Multifunctional Materials in Heterogeneous Catalysis. *Adv. Energy Mater.* **2018**, *8*, 1701343.

(5) Campbell, C. T.; Parker, S. C.; Starr, D. E. The Effect of Size-Dependent Nanoparticle Energetics on Catalyst Sintering. *Science* **2002**, *298*, 811–814.

(6) Ouyang, R.; Liu, J. X.; Li, W. X. Atomistic Theory of Ostwald Ripening and Disintegration of Supported Metal Particles under Reaction Conditions. *J. Am. Chem. Soc.* **2013**, *135*, 1760–1771.

(7) Prieto, G.; Zecevic, J.; Friedrich, H.; de Jong, K. P.; de Jongh, P. E. Towards Stable Catalysts by Controlling Collective Properties of Supported Metal Nanoparticles. *Nat. Mater.* **2013**, *12*, 34–39.

(8) Yuan, S.; Chen, Y.-P.; Qin, J.; Lu, W.; Wang, X.; Zhang, Q.; Bosch, M.; Liu, T.-F.; Lian, X.; Zhou, H. C. Cooperative Cluster Metalation and Ligand Migration in Zirconium Metal-Organic Frameworks. *Angew. Chem., Int. Ed.* **2015**, *54*, 14696–14700.

(9) Li, Z.; Peters, A. W.; Bernales, V.; Ortuno, M. A.; Schweitzer, N. M.; DeStefano, M. R.; Gallington, L. C.; Platero-Prats, A. E.; Chapman, K. W.; Cramer, C. J. Metal-Organic Framework Supported Cobalt Catalysts for the Oxidative Dehydrogenation of Propane at Low Temperature. *ACS Cent. Sci.* **2017**, *3*, 31–38.

(10) Kim, I. S.; Li, Z.; Zheng, J.; Platero-Prats, A. E.; Mavrandonakis, A.; Pellizzeri, S.; Ferrandon, M.; Vjunov, A.; Gallington, L. C.; Webber, T. E.; Vermeulen, N. A.; Penn, R. L.; Getman, R. B.; Cramer, C. J.; Chapman, K. W.; Camaioni, D. M.; Fulton, J. L.; Lercher, J. A.; Hupp, J. T.; Farha, O. K.; Martinson, A. B. F. Sinter-Resistant Platinum Catalyst Supported by Metal-Organic Framework. *Angew. Chem., Int. Ed.* **2018**, *57*, 909–913.

(11) Yaghi, O. M.; O’Keeffe, M.; Ockwig, N. W.; Chae, H. K.; Eddaoudi, M.; Kim, J. Reticular Synthesis and the Design of New Materials. *Nature* **2003**, *423*, 705–714.

(12) Li, Z.; Schweitzer, N. M.; League, A. B.; Bernales, V.; Peters, A. W.; Getsoian, A. B.; Wang, T. C.; Miller, J. T.; Vjunov, A.; Fulton, J. L. Sintering-Resistant Single-Site Nickel Catalyst Supported by Metal-Organic Framework. *J. Am. Chem. Soc.* **2016**, *138*, 1977–1982.

(13) Metzger, E. D.; Brozek, C. K.; Comito, R. J.; Dinca, M. Selective Dimerization of Ethylene to 1-Butene with a Porous Catalyst. *ACS Cent. Sci.* **2016**, *2*, 148–153.

(14) Manna, K.; Ji, P.; Lin, Z.; Greene, F. X.; Urban, A.; Thacker, N. C.; Lin, W. Chemoselective single-site Earth-Abundant Metal Catalysts at Metal-Organic Framework Nodes. *Nat. Commun.* **2016**, *7*, 12610.

(15) Rungtaweivoranit, B.; Baek, J.; Araujo, J. R.; Archanjo, B. S.; Choi, K. M.; Yaghi, O. M.; Somorjai, G. A. Copper Nanocrystals Encapsulated in Zr-based Metal-Organic Frameworks for Highly Selective CO<sub>2</sub> Hydrogenation to Methanol. *Nano Lett.* **2016**, *16*, 7645–7649.

(16) Zhao, M.; Yuan, K.; Wang, Y.; Li, G.; Guo, J.; Gu, L.; Hu, W.; Zhao, H.; Tang, Z. Metal-Organic Frameworks as Selectivity Regulators for Hydrogenation Reactions. *Nature* **2016**, *539*, 76–80.

(17) Platero-Prats, A. E.; Li, Z.; Gallington, L. C.; Peters, A. W.; Hupp, J. T.; Farha, O. K.; Chapman, K. W. Addressing the Characterisation Challenge to Understand Catalysis in MOFs: the Case of Nanoscale Cu Supported in NU-1000. *Faraday Discuss.* **2017**, *201*, 337–350.

(18) An, B.; Zhang, J.; Cheng, K.; Ji, P.; Wang, C.; Lin, W. Confinement of Ultrasmall Cu/ZnO<sub>x</sub> Nanoparticles in Metal-Organic Frameworks for Selective Methanol Synthesis from Catalytic Hydrogenation of CO<sub>2</sub>. *J. Am. Chem. Soc.* **2017**, *139*, 3834–3840.

- (19) Gutterød, E. S.; Øien-Ødegaard, S.; Bossers, K.; Nieuwelink, A. E.; Manzoli, M.; Braglia, L.; Lazzarini, A.; Borfecchia, E.; Ahmadigoltapeh, S.; Bouchevreau, B.; Lonstad-Bleken, B. T.; Henry, R.; Lamberti, C.; Bordiga, S.; Weckhuysen, B. M.; Lillerud, K. P.; Olsbye, U. CO<sub>2</sub> Hydrogenation over Pt-Containing UiO-67 Zr-MOFs-The Base Case. *Ind. Eng. Chem. Res.* **2017**, *56*, 13206–13218.
- (20) Lubitz, W.; Tumas, W. Hydrogen: An Overview. *Chem. Rev.* **2007**, *107*, 3900–3903.
- (21) Weisz, P. B. Intraparticle diffusion in catalytic systems. *Chem. Engin. Progr. Symp. Ser.* **1992**, *55*, 29–36.
- (22) Kokoric, V.; Widmann, D.; Wittmann, M.; Behm, R. J.; Mizaikoff, B. Infrared Spectroscopy via Substrate-Integrated Hollow Waveguides: A Powerful Tool in Catalysis Research. *Analyst* **2016**, *141*, 5990–5995.
- (23) Schubert, M. M.; Häring, T. P.; Bräth, G.; Gasteiger, H. A.; Behm, R. J. New DRIFTS Cell Design for the Simultaneous Acquisition of IR Spectra and Kinetic Data Using On-line Product Analysis. *Appl. Spectrosc.* **2001**, *55*, 1537–1543.
- (24) Hamadeh, I. M.; King, D.; Griffiths, P. R. Heatable-Evacuable Cell and Optical System for Diffuse Reflectance FT-IR Spectrometry of Adsorbed Species. *J. Catal.* **1984**, *88*, 264–272.
- (25) Eckle, S.; Augustin, M.; Anfang, H.-G.; Behm, R. J. Influence of the Catalyst Loading on the Activity and the CO Selectivity in the Selective Methanation of CO in CO<sub>2</sub> containing Feed Gases over Ru Supported Catalysts. *Catal. Today* **2012**, *181*, 40–51.
- (26) Newville, M. IFEFFIT: interactive XAFS analysis and FEFF fitting. *J. Synchrotron Radiat.* **2001**, *8*, 322–324.
- (27) Koningsberger, D. C.; Mojet, B. L.; van Dorssen, G. E.; Ramaker, D. E. XAFS Spectroscopy; Fundamental Principles and Data Analysis. *Top. Catal.* **2000**, *10*, 143–155.
- (28) Bordiga, S.; Groppo, E.; Agostino, G.; van Bokhoven, J. A.; Lamberti, C. Reactivity of Surface Species in Heterogeneous Catalysts Probed by In Situ X-ray Absorption Techniques. *Chem. Rev.* **2013**, *113*, 1736–1850.
- (29) Ankudinov, A. L.; Ravel, B.; Rehr, J. J.; Conradson, S. D. Real-Space Multiple-Scattering Calculation and Interpretation of X-ray Absorption Near-Edge Structure. *Phys. Rev. B: Condens. Matter Mater. Phys.* **1998**, *58*, 7565–7576.
- (30) Trickett, C. A.; Gagnon, K. J.; Lee, S.; Gandara, F.; Bürgi, H. B.; Yaghi, O. M. Definitive Molecular Level Characterization of Defects in UiO-66 Crystals. *Angew. Chem., Int. Ed.* **2015**, *54*, 11162–11167.
- (31) Valenzano, L.; Civalieri, B.; Chavan, S.; Bordiga, S.; Nilsen, M. H.; Jakobsen, S.; Lillerud, K. P.; Lamberti, C. Disclosing the Complex Structure of UiO-66 Metal Organic Framework: a Synergic Combination of Experiment and Theory. *Chem. Mater.* **2011**, *23*, 1700–1718.
- (32) Ling, S.; Slater, B. Dynamic Acidity in Defective UiO-66. *Chem. Sci.* **2016**, *7*, 4706–4712.
- (33) Yang, D.; Ortuno, M. A.; Bernales, V.; Cramer, C. J.; Gagliardi, L.; Gates, B. C. Structure and Dynamics of Zr<sub>6</sub>O<sub>8</sub> Metal-Organic Framework Node Surfaces Probed with Ethanol Dehydration as a Catalytic Test Reaction. *J. Am. Chem. Soc.* **2018**, *140*, 3751–3759.
- (34) Farrauto, R.; Heck, R. M. Catalytic Converters: State of the Art and Perspectives. *Catal. Today* **1999**, *51*, 351–360.
- (35) Morales, F.; Viniegra, M.; Arroyo, R.; Cordoba, G.; Zepeda, T. A. CO oxidation Over CuO/ZrO<sub>2</sub> Catalysts: Effect of Loading and Incorporation Procedure of CuO. *Mater. Res. Innovations* **2010**, *14*, 183–188.
- (36) Li, Y.; Cai, Y.; Xing, X.; Chen, N.; Deng, D.; Wang, Y. Catalytic Activity for CO Oxidation of Cu-CeO<sub>2</sub> Composite Nanoparticles Synthesized by a Hydrothermal Method. *Anal. Methods* **2015**, *7*, 3238–3245.
- (37) Bera, P.; Patil, K. C.; Jayaram, V.; Subbanna, G. N.; Hegde, M. S. Ionic Dispersion of Pt and Pd on CeO<sub>2</sub> by Combustion Method: Effect of Metal-Ceria Interaction on Catalytic Activities for NO Reduction and CO and Hydrocarbon Oxidation. *J. Catal.* **2000**, *196*, 293–301.
- (38) Kahlich, M. J.; Gasteiger, H. A.; Behm, R. J. Kinetics of the Selective CO Oxidation in H<sub>2</sub>-rich Gas on Pt/Al<sub>2</sub>O<sub>3</sub>. *J. Catal.* **1997**, *171*, 93–105.
- (39) Kahlich, M. J.; Gasteiger, H. A.; Behm, R. J. Kinetics of the Selective Low-Temperature Oxidation of CO in H<sub>2</sub>-rich Gas over Au/a-Fe<sub>2</sub>O<sub>3</sub>. *J. Catal.* **1999**, *182*, 430–440.
- (40) Hadjiivanov, K.; Knözinger, H. FTIR study of CO and NO Adsorption and Coadsorption on a Cu/SiO<sub>2</sub> catalyst: Probing the Oxidation State of Copper. *Phys. Chem. Chem. Phys.* **2001**, *3*, 1132–1137.
- (41) Giordanino, F.; Vennestrom, P. N. R.; Lundegaard, L. F.; Stappen, F. N.; Mossin, S.; Beato, P.; Bordiga, S.; Lamberti, C. Characterization of Cu-Exchanged SSZ-13: a Comparative FTIR, UV-Vis, and EPR study with Cu-ZSM-5 and Cu-b with Similar Si/Al and Cu/Al ratios. *Dalton Trans.* **2013**, *42*, 12741–12761.
- (42) Hadjiivanov, K.; Knözinger, H. FTIR Study of Low-Temperature CO Adsorption on Cu-ZSM-5: Evidence of the Formation of Cu<sup>2+</sup>(CO)<sub>2</sub> Species. *J. Catal.* **2000**, *191*, 480–485.
- (43) Okamoto, Y.; Kubota, T.; Gotoh, H.; Ohto, Y.; Aritani, H.; Tanaka, T.; Yoshida, S. XAFS Study of Zirconia-Supported Copper Catalysts for the NO-CO Reaction: Deactivation, Rejuvenation and Stabilization of Cu Species. *J. Chem. Soc., Faraday Trans.* **1998**, *94*, 3743–3752.
- (44) Caballero, A.; Morales, J. J.; Cordon, A. M.; Holgado, J. P.; Espinos, J. P.; Gonzalez-Elipe, A. R. An In Situ XAS study of Cu/ZrO<sub>2</sub> Catalysts Under de-NO<sub>x</sub> Reaction Conditions. *J. Catal.* **2005**, *235*, 295–301.
- (45) Muddada, N. B.; Olsbye, U.; Leofanti, G.; Gianolio, D.; Bonino, F.; Bordiga, S.; Fuglerud, T.; Vidotto, S.; Marsella, A.; Lamberti, C. Quantification of Copper Phases, Their Reducibility and Dispersion in Doped-CuCl<sub>2</sub>/Al<sub>2</sub>O<sub>3</sub> Catalysts for Ethylene Oxidation. *Dalton Trans.* **2010**, *39*, 8437–8449.
- (46) Su, Y.; Brown, H. M.; Li, G.; Zhou, X. D.; Amonette, J. E.; Fulton, J. L.; Camaioni, D. M.; Zhang, Z. C. Accelerated Cellulose Depolymerization Catalyzed by Paired Metal Chlorides in Ionic Liquid Solvent. *Appl. Catal., A* **2011**, *391*, 436–442.
- (47) Chakhalian, J.; Freeland, J. W.; Habermeier, H. U.; Cristiani, G.; Khalilullin, G.; Van Veenendaal, M.; Keimer, B. Orbital Reconstruction and Covalent Bonding at an Oxide Interface. *Science* **2007**, *318*, 1114–1117.
- (48) Larsson, S. Theory of Satellite Excitations in Inner Shell X-ray Photoelectron Spectra of Nickel and Copper Compounds. *Chem. Phys. Lett.* **1975**, *32*, 401–406.
- (49) Larsson, S. Shake-up and Multiplet Structure of ESCA Satellites of Cu Compounds. *Chem. Phys. Lett.* **1976**, *40*, 362–366.
- (50) Ghijsen, J.; Tjeng, L. H.; Van Elp, J.; Eskes, H.; Westerink, J.; Sawatzky, G. A.; Czyzyk, M. T. Electronic Structure of Cu<sub>2</sub>O and CuO. *Phys. Rev. B: Condens. Matter Mater. Phys.* **1988**, *38*, 11322.